JOURNAL OF SYNCHROTRON RADIATION

ISSN 1600-5775

Magnetic design and modelling of a 14 mm-period prototype superconducting undulator

G. Mishra,[a] Mona Gehlot,[a]* Geetanjali Sharma[b] and Frederic Trillaud[c]

[a]IDDL, Devi Ahilya University, Indore, MP 452001, India, [b]Synchrotron Soleil, Paris, France, and [c]Institute of Engineering, UNAM, Mexico. *Correspondence e-mail: mona_gehlot@yahoo.com

Received 14 November 2016
Accepted 30 January 2017

Edited by M. Eriksson, Lund University, Sweden

Keywords: superconducting undulator.

The magnetic design of a ten-period (each period 14 mm) prototype superconducting undulator is reported using *RADIA*. The results of modelling the magnetic flux density are presented in an analytical formula. The dependence of the field integrals and phase error on the current density and undulator gap has been calculated, and temperature curves are determined for the models and are compared with earlier reported Moser–Rossmanith fits.

1. Introduction

In recent years there has been increasing interest in superconducting undulator technology for synchrotron radiation and free-electron lasers applications (Kim *et al.*, 2003; Trakhtenberg *et al.*, 2010; Ivanyushenkov *et al.*, 2012, 2014, 2015; Dietderich *et al.*, 2007; Hezel *et al.*, 1999; Boffo *et al.*, 2010; Hwang *et al.*, 2006; Moser & Rossmanith, 2002; Grau *et al.*, 2010, 2011; Mashkina *et al.*, 2008*a*,*b*; Kostka *et al.*, 2004). Superconducting undulator yields have shown improved performance over normal conducting electromagnetic wigglers and permanent magnet undulators. Superconducting undulators are built using coils wound with superconducting commercially available NbTi or Nb_3Sn wires, which are cooled down to cryogenic temperatures typically between 1.8 K and 6 K. In this temperature range they produce stronger magnetic fields due to their ability to carry larger current densities without electrical losses. Higher magnetic flux density in superconducting undulators allows the reduction in undulator length, which is often desired for table-top compact new generation free-electron laser facilities. A short period and simpler K tuning through current in the coils are further attractive features in comparison with the massive adjustable gap and adjustable phase for pure permanent magnet and hybrid undulators. Over the years interest and efforts have grown, with several superconducting undulators built and operated successfully at 4.2 K. The superconducting undulator technology has been effectively implemented in the design of transverse-gradient undulators and superconducting undulators with variable polarizations (Afonso Rodriguez *et al.*, 2013; Emma *et al.*, 2014; Chen *et al.*, 2009, 2010).

In this paper we report the design of a 14 mm-period superconducting undulator at the Insertion Device Development Laboratory, DAVV, Indore, India. The field computations are performed using *RADIA* (Wallén *et al.*, 2005; Wallén, 2002). The *RADIA* results are presented in analytical form for magnetic flux density computations on-axis and on the surface of the coil. In §2, the mechanical design of the superconducting undulator is presented with rectangular cross-sectional wire.

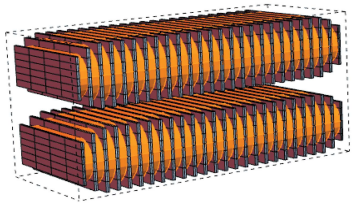

The performance of the superconducting undulator through the field integrals and the phase error from the *RADIA* model are presented in §3 and §4. The present analytical fit is analyzed for the superconducting undulator for a wide range of current densities and undulator gaps. A brief discussion of the model in terms of field integrals, phase error and temperature curves is presented in §5.

2. Superconducting magnetic design layout

Commercial NbTi wires with a cross section of 1 mm × 0.5 mm including insulation are used for fabrication of the 14 mm-period superconducting undulator (SCU). The undulators are composed of racetrack coils connected in series and wound on two ferromagnetic poles made of carbon steel.

The SCU consists of 26 poles and 25 coils which are numbered from 1 to 51. Fig. 1 shows a longitudinal view of the pole–coils of the superconducting undulator. The regular pole is 2 mm in length (beam direction), 40 mm in width (undulating direction) and 8 mm in height (vertical direction). The regular coil length with five turns is 5 mm (5 turns × 1 mm) and the coil height with 16 layers is 8 mm (16 layers × 0.5 mm). The undulator begins with a pole and follows a pole–coil–pole arrangement numbered from 1 to 51, ending with a pole in an asymmetric field configuration. The end field configuration in the scheme is 1:3/4:1/4. The end poles–coils are numbered 1–2–3–4 at the left end and 48–49–50–51 at the right end. The poles–coils numbered from 5 to 47 are regular in size. End pole 1 is 1.6 mm in length and pole 3 is 1.96 mm in length. The coils numbered 3 and 4 are 5 mm in length. Poles 1 and 3 are 2 mm (1/4) and 6 mm (3/4) in height, respectively. Coil 2 is 2 mm in height (0.5 mm × 4) and coil 4 is 6 mm in height (0.5 mm × 12). The total length of the magnetic structure {22 regular poles = 44 mm, 21 coils = 105 mm, end design = 2 × 13.56 mm [2 × (1.6 mm + 5 mm + 1.96 mm + 5 mm)]} is 176.12 mm. Fig. 2 presents a longitudinal view of the complete superconducting undulator pole–core assembly.

3. Field integrals

The important quantities for quality undulators are its field integrals. The field integrals are calculated directly from the magnetic field mapping. The integrals defined through

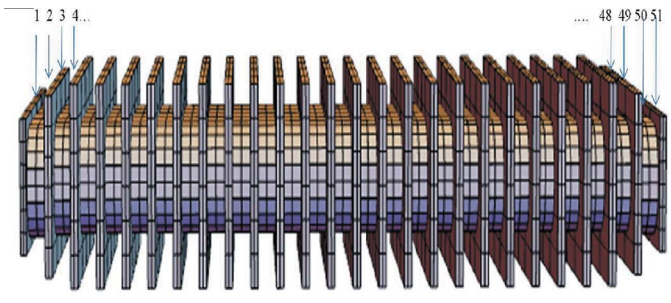

Figure 1
Cross section of the pole–coil of the SCU.

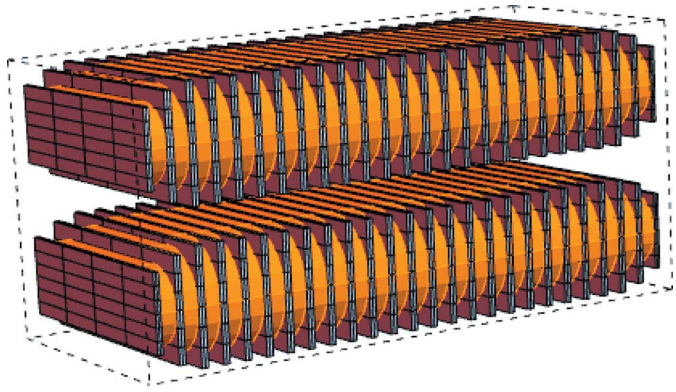

Figure 2
Longitudinal view of the SCU with end termination.

$$I_1 = \int_0^z B_y(\xi)\,\mathrm{d}\xi, \qquad I_2 = \int_0^z I_1(\xi)\,\mathrm{d}\xi \tag{1}$$

are called the first and second field integrals, respectively. These integrals are proportional to the angular position and displacement of the electron beam at the undulator exit. The above equations, when multiplied by $-e/(\gamma mc)$, give the angular and trajectory offset. Setting $-e/mc = 565\ \mathrm{T^{-1}\ m^{-1}}$ and $\gamma = 1957E$ (GeV), we obtain

$$\frac{-e}{\gamma mc} = \frac{0.298}{E\,[\mathrm{GeV}]}\ \left[\mathrm{T^{-1}\ m^{-1}}\right]. \tag{2}$$

The dimensions of the poles and coils are used in *RADIA* to estimate the performance of the proto-SCU. The magnetic flux density at a gap of 3–11 mm is plotted in Fig. 3 for a current density of 800 A mm $^{-2}$. The analysis predicts a field of >1 T for a 5 mm gap. The first field integral and the second field integral *versus* gap and current density have been evaluated and are plotted in Figs. 4 and 5. In Figs. 6–8 the gap is held at 5 mm and the current density is varied from 600 to 1400 A mm^{-2}.

The results in Figs. 3 and 6 are compiled in Fig. 9 to estimate the magnetic flux density *versus* gap for different current densities. Fig. 10 plots the magnetic flux density *versus* current

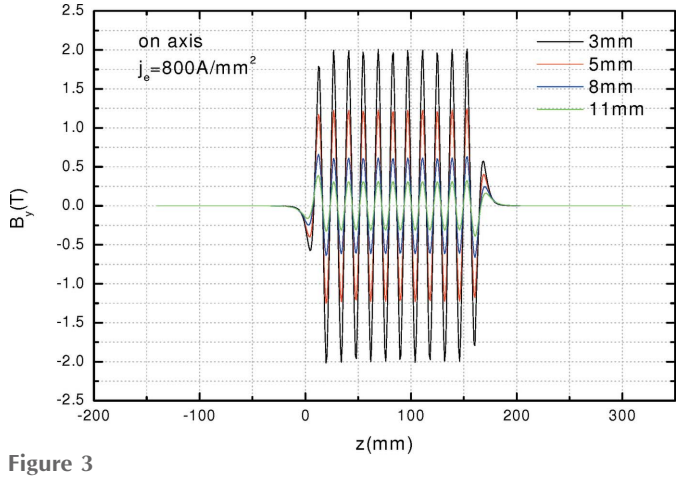

Figure 3
Magnetic flux density *versus* longitudinal position.

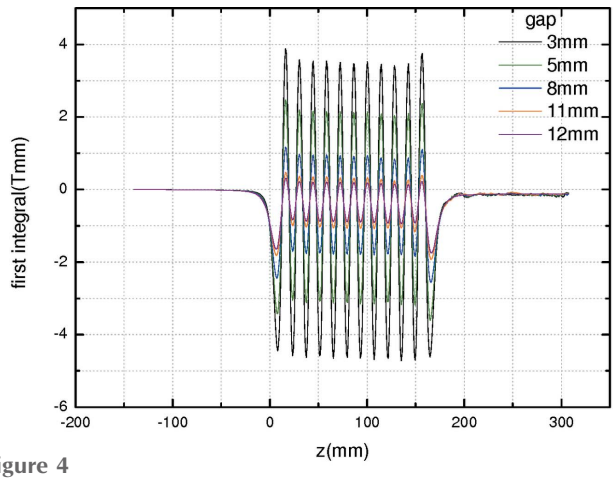

Figure 4
First field integral for different gaps at a current density of 800 A mm^{-2}.

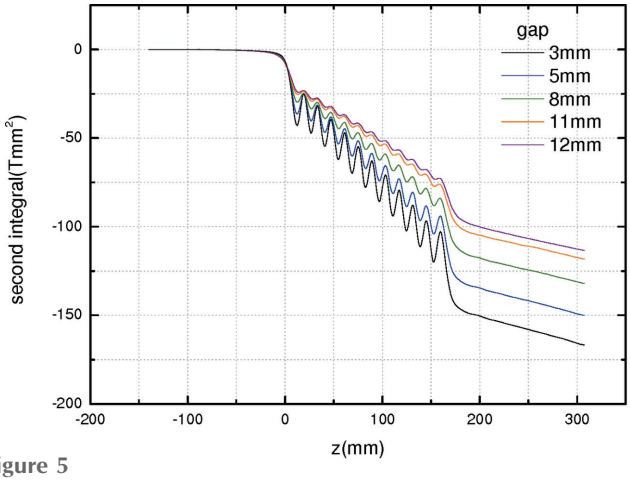

Figure 5
Second field integral for different gaps at a current density of 800 A mm^{-2}.

density at various gaps. The magnetic flux density at the surface of the coil is shown in Figs. 11 and 12 for different gaps at different current densities.

The field integrals *versus* current density are plotted in Fig. 13 at gaps of 3 to 11 mm. The field integrals show a maximum value in the 825–950 A mm^{-2} range with decreasing values at wider gaps. The gap dependence of the field integrals (Tischer & Pflueger, 2000) in permanent magnet undulators often describe a bump pattern. The field integral is maximum at a particular gap and decreases at other gaps. The present SCU model shares this important analogy with the permanent undulator. The left-hand axis of the plot corresponds to the value of the first field integral; the right-hand axis corresponds to second field integral values. The field integral values are taken at a longitudinal point close to the structure (z = 195 mm). The first field integral shows a dip at ~850 A mm^{-2}. Increasing the current density beyond this point, the magnetic flux density increases, while decreasing the current density from this value results in the magnetic flux density decreasing. The sudden dip at 850 A mm^{-2} corresponds to imperfect magnetic flux density with unequal slopes and to a mismatch end design. By decreasing the gap between the coils the

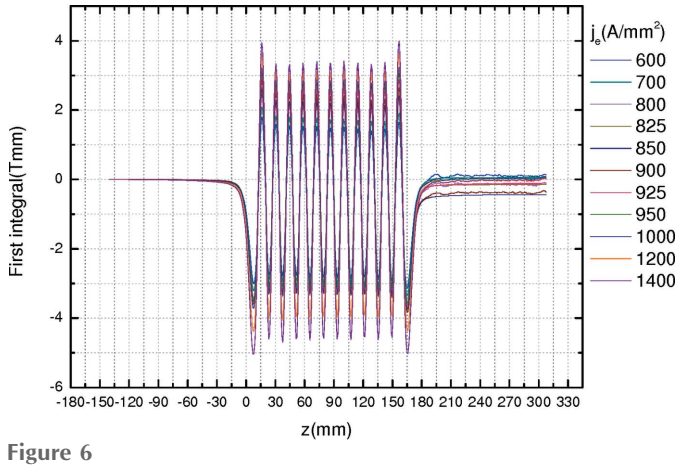

Figure 6
First field integral with different current densities for a 5 mm gap.

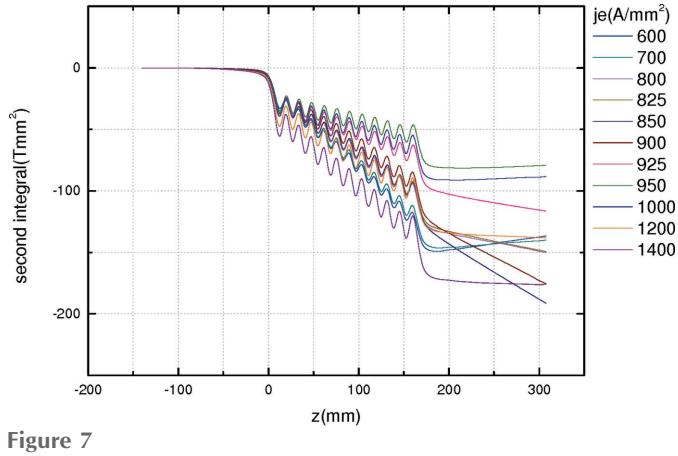

Figure 7
Second field integral for different current densities for a 5 mm gap.

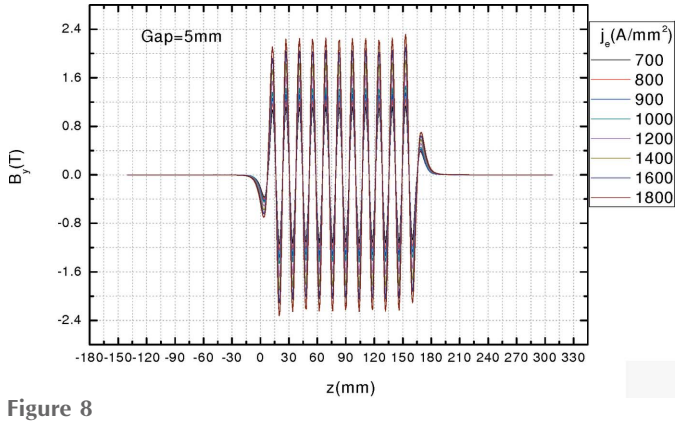

Figure 8
Magnetic flux density *versus* longitudinal position at several current densities.

magnetic flux density decreases; the slope flattens causing the dip to flatten. The results show minimum first field integrals of 0.01414 T mm (5 mm gap) and 0.00417 T mm (8 mm gap) at ~1000 A mm^{-2}. This corresponds to 1.68 µrad and 0.5 µrad at 5 mm and 8 mm gaps, respectively. The second field integral shows minimum values of 10.8 µm and 10.25 µm at 5 mm and 8 mm gaps, respectively. Both calculations were carried out at a beam energy of 2.5 GeV.

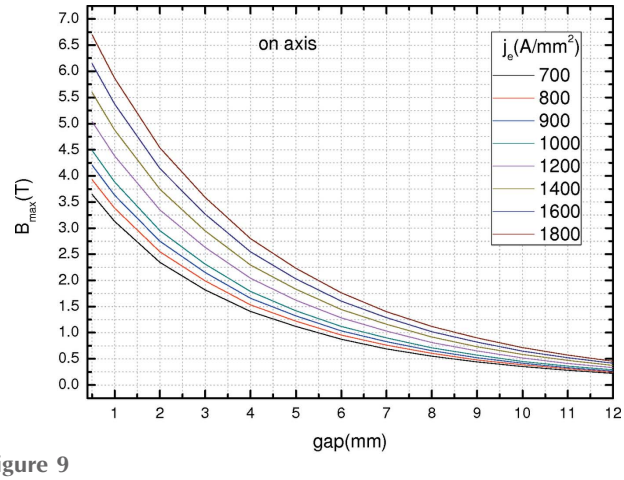

Figure 9
Magnetic flux density *versus* gap at different current densities.

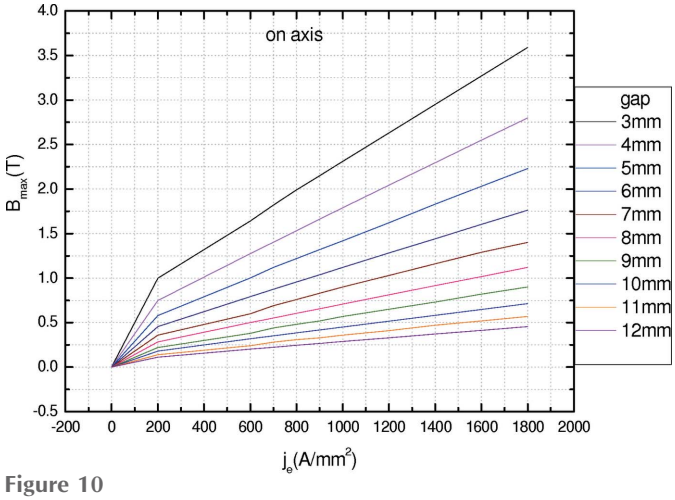

Figure 10
Magnetic flux density *versus* current density at different gaps.

4. Phase error

The phase errors (Diviacco & Walker, 1996; Bilani *et al.*, 2014; Chunjarean *et al.*, 2011) estimate the overall impact of the undulator on the electron beam and are the most useful parameters for undulator selection and optimization for its implementation in a free-electron laser. It can be derived from the phase slip between an electron and light wave. The electron longitudinal velocity is given by

$$\frac{1}{u_z} = \frac{1}{c}\left[1 + \frac{1}{2\gamma^2} + \frac{\beta_z^2}{2}\left(\frac{dx}{dz}\right)^2\right]. \quad (3)$$

The slip between the electron and light wave is given by $s(z) = c\Delta t$, where

$$\Delta t = \int_0^z \left(\frac{1}{u_z} - \frac{1}{c}\right) \mathrm{d}\xi. \quad (4)$$

Equation (4) is solved with the aid of equation (3) as follows,

$$s(z) = \frac{1}{2\gamma^2}\left[z + \frac{e^2}{m^2c^2} J(z)\right], \qquad J(z) = \int_0^z I_1^2(\xi)\,\mathrm{d}\xi. \quad (5)$$

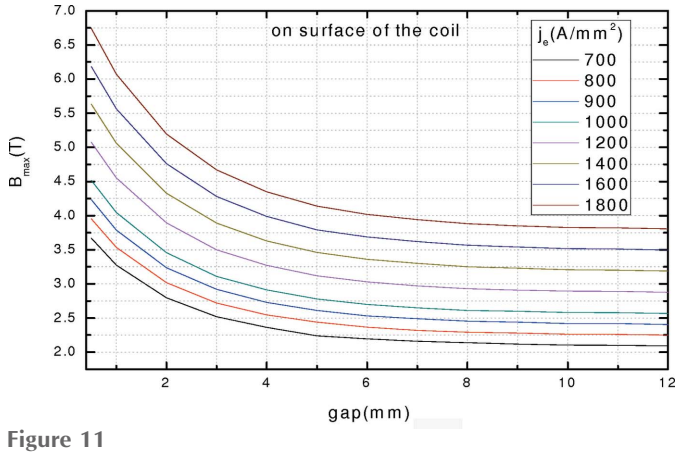

Figure 11
Magnetic flux density *versus* gap at the surface of the coil.

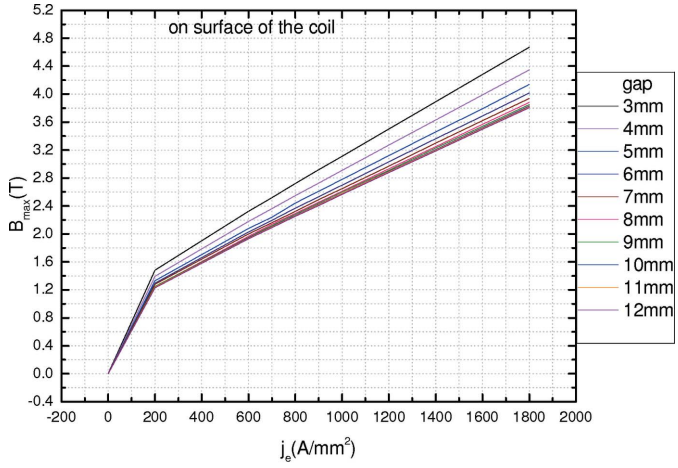

Figure 12
Magnetic flux density *versus* current density at the surface of the coil.

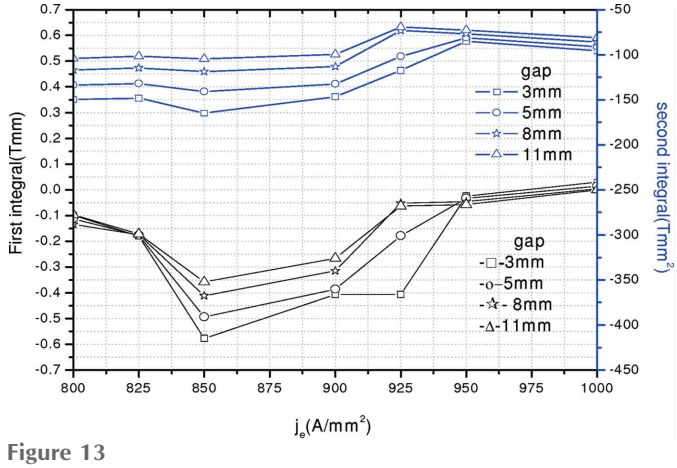

Figure 13
First and second field integrals *versus* current density.

The phase difference between the photon and the electron, *i.e.* $\Delta\varphi(z)$ in radians, is defined as the difference between $s(z)$ (in units of λ) and z (in units of λ_u),

$$\Delta\varphi(z) = 2\pi\left[\frac{s(z)}{\lambda} - \frac{z}{\lambda_u}\right]. \quad (6)$$

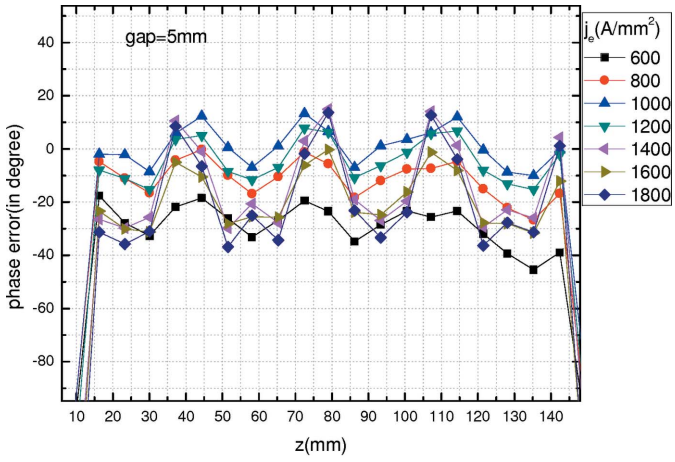

Figure 14
Phase error at a gap of 5 mm.

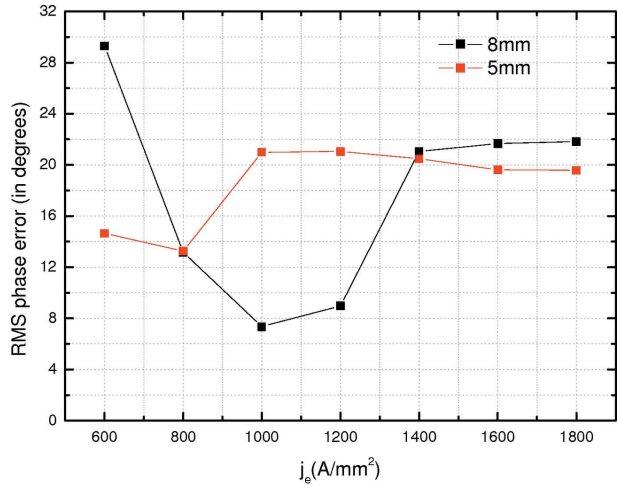

Figure 15
RMS phase error *versus* current density at 5 mm and 8 mm gaps.

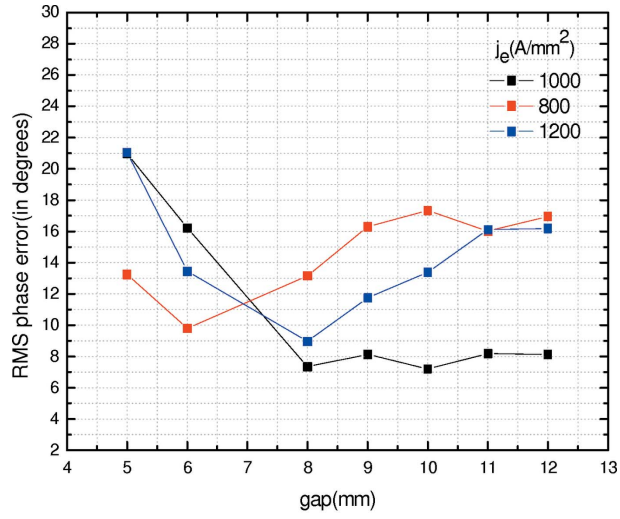

Figure 16
RMS phase error *versus* gap at different current densities.

Equation (6) is used to evaluate the phase error. The phase error is related to magnetic field errors along the length of the undulator. Field variations up to 0.02 T are observed in the design and are likely to yield large phase errors. The plot in Fig. 14 shows calculated phase errors associated with the designed SCU at different current densities at a gap of 5 mm. The RMS phase error is around 21° at 5 mm gap at 1000 A mm^{-2} and decreases to 7° at 8 mm gap at the same current density. The important effects of the gap dependence of the RMS phase error are shown in Figs. 15 and 16 for three different current densities. To achieve a decrease in the phase error in the SCU design one needs to increase the operating gap of the device. The phase error remains at 7° for gaps from 8 mm to 12 mm.

5. Results and discussion

The design details and magnetic performance of a proposed proto-SCU structure have been discussed. The code *RADIA* has been used extensively for the estimated performance of the proposed device. The calculations were carried out with λ_u = 14 mm and a pole length of 2 mm. The magnetic flux density of a hybrid undulator is specified by $B_{\rm axis}(T) = a(B_r)\exp[-b(B_r)g + c(B_r)g^2]$, where the coefficients a, b, c are fixed by the material used in the fabrication of the hybrid structure and B_r is the remanent field of the undulator magnets (Jia *et al.*, 2004). In analogy with the above formula, Figs. 9 and 10 provide an analytical estimate of the magnetic flux density as

$$B_{\rm axis}(T) = a(J_e)\exp\left[-b(J_e)\,g + c(J_e)\,g^2\right], \qquad (7)$$

where

$$a(J_e) = 2.018 + 0.0031J_e,$$
$$b(J_e) = 0.24731 + 0.10436\exp(-0.0012\,J_e),$$
$$c(J_e) = 0.00142 + 0.00682\exp(-0.0012\,J_e).$$

In the above formulae, the units for g are mm and those for current density (J_e) are A mm^{-2}. Moser & Rossmanith (2002) reported an empirical fit using the code *SRW* (developed by ESRF) to calculate the magnetic flux density from an analytical formula for the superconducting structure. The model compared the results with the field obtained from a pure permanent magnet undulator. The present empirical formula is compared with the Moser formula and the results are discussed in detail by Gehlot *et al.* (2017) for the range of current densities and undulator gaps of interest. The *RADIA* results for the magnetic flux density on the surface of the coil in Figs. 11 and 12 can be set through an empirical fit as

$$B_{\rm coil}(T) = A_1(J_e) + A_2(J_e)\exp\left[-B(J_e)\,g\right], \qquad (8)$$

where

$$A_1(J_e) = 1.02017 + 0.00155\,J_e,$$
$$A_2(J_e) = 0.93484 + 0.00155\,J_e,$$
$$B(J_e) = 0.4807 + 0.12691\exp(-0.0015\,J_e).$$

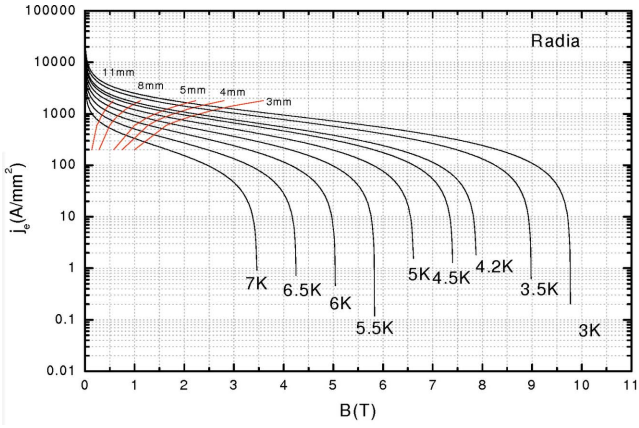

Figure 17
Current density *versus* magnetic flux density from *RADIA* calculations.

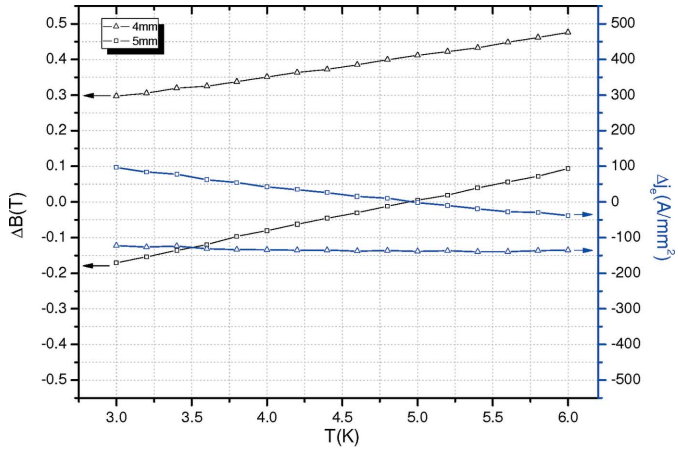

Figure 19
Difference in magnetic field and current density *versus* temperature.

The operating temperature range and the load curves of the proposed device are analyzed in Fig. 17. The load lines are drawn from the Gehlot *et al.* (2017) fit; the temperature curves are drawn from the Bottura equations. The load lines in Fig. 18 are drawn from the Moser–Rossmanith fit formula. Fig. 19 compares the effects from both fits. The difference in the magnetic flux density and the operating current density of both fits are investigated in the temperature range from 3 to 6 K. At a temperature of 4.2 K, the difference flux densities are 0.36 T (4 mm gap) and 0.05 T (5 mm gap). The respective difference in operating current density is 136 A mm^{-2} (4 mm) and 30 A mm^{-2} (5 mm).

Acknowledgements

This work is supported by SERB-DST grant EMR/2014/00120. MG acknowledges financial support from UGC [No. F.15-1/2014-15/PDFWM-2014-15-GE-MAD-26801 (SA-II)], Delhi, and the Government of India to carry out the simulation study presented in the manuscript. FT thanks the DGAPA of the National Autonomous University of Mexico for financial support provided through grant TA100617.

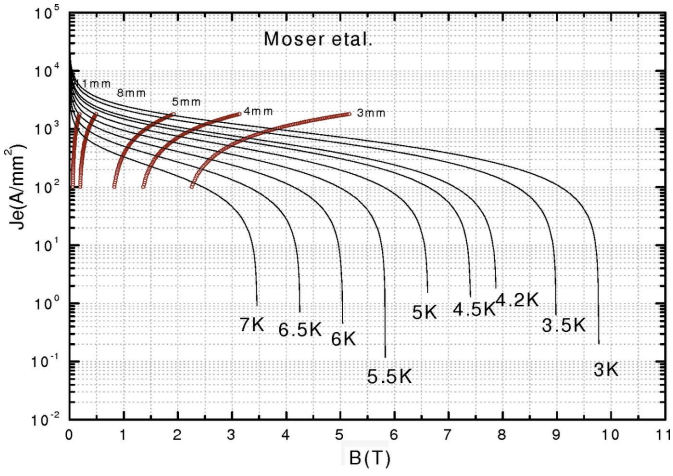

Figure 18
Current density *versus* magnetic flux density from the Moser formula.

References

Afonso Rodriguez, V., Bernhard, A., Keilmann, A., Peiffer, P., Rossmanith, R., Widmann, C., Baumbach, T., Nicolai, M. & Kaluza, M. C. (2013). *IEEE Trans. Appl. Supercond.* **23**, 4101505.

Bilani, O., Neumann, P., Schöps, A., Tischer, M., Tripathi, S., Vagin, P. & Vielitz, T. (2014). *Proceedings of the 5th International Particle Accelerator Conference (IPAC-2014)*, 15–20 June 2014, Dresden, Germany. TUPRO084.

Boffo, C., Walter, W., Baumbach, T., Casalbuoni, S., Grau, A. W., Hagelstein, M. & Saez de Jauregui, D. (2010). *Proceedings of the First International Particle Accelerator Conference (IPAC'10)*, 23–28 May 2010, Kyoto, Japan. WEPD021.

Chen, S. D., Jan, J. C., Hwang, C. S. & Liang, K. S. (2010). *J. Phys. Conf. Ser.* **234**, 032006.

Chen, S. D., Jan, J. C., Hwang, C. S. & Liang, K. S. (2009). *9th European Conference on Applied Superconductivity (EUCAS'09)*, 13–17 September 2009, Dresden, Germany.

Chunjarean, S., Hwang, C. S. & Wiedemann, H. (2011). *Proceedings of the Second International Particle Accelerator Conference (IPAC'11)*, 4–9 September 2011, San Sebastian, Spain, p. 3290.

Dietderich, D., Godeke, A., Prestemon, S. O., Pipersky, P. T., Liggins, N. L., Higley, H. C., Marks, S. & Schlueter, R. D. (2007). *IEEE Trans. Appl. Supercond.* **17**, 1243–1246.

Diviacco, B. & Walker, R. (1996). *Nucl. Instrum. Methods Phys. Res. A*, **368**, 522–532.

Emma, P., Holtkamp, N. R., Nuhn, H.-D., Arbelaez, D., Corlett, J. N., Myers, S. A., Prestemon, S., Schlueter, D., Doose, C. L., Fuerst, J. D., Gluskin, E., Hasse, Q. B., Ivanyushenkov, Y., Kasa, M., Pile, G. & Trakhtenberg, E. (2014). *Proceedings of the 36th International Free Electron Laser Conference*, 25–29 August 2014, Basel, Switzerland, p. 649. THA 03.

Gehlot, M., Mishra, G., Trillaud, F. & Sharma, G. (2017). *Nucl. Instrum. Methods Phys. Res. A*, **846**, 13–17.

Grau, A. W. Baumbach, T., Casalbuoni, S., Gerstl, S., Hagelstein, M., Holubek, T. & Saez de Jauregui, D. (2011). *Proceedings of the Second International Particle Accelerator Conference (IPAC'11)*, 4–9 September 2011, San Sebastian, Spain, pp. 3275–3277. THPC163.

Grau, A. W., Baumbach, T., Casalbuoni, S., Gerstl, S., Hagelstein, M. & Saez de Jauregui, D. (2010). *Proceedings of the First International Particle Accelerator Conference (IPAC'10)*, 23–28 May 2010, Kyoto, Japan, pp. 3129–3131. WEPD019.

Hezel, T., Homscheidt, M., Moser, H. O., Rossmanith, R., Schneider, T., Backe, H., Dambach, S., Hagenbuck, F., Kaiser, K.-H., Kube, G., Lauth, W., Steinhof, A. & Walcher, T. (1999). *Proceedings of the 1999 Particle Accelerator Conference*, 27 March–2 April 1999, New York, USA, pp. 165–167.

Hwang, C. S., Jan, J. C., Lin, P. H., Chang, C. H., Huang, M. H., Lin, F. Y., Fan, T. C. & Chen, H. H. (2006). *IEEE Trans. Appl. Supercond.* **16**, 1855–1858.

Ivanyuschenkov, Y. *et al.* (2014). *Proceedings of the 5th International Particle Accelerator Conference (IPAC-2014)*, 15–20 June 2014, Dresden, Germany. WEPRO048.

Ivanyuschenkov, Y. *et al.* (2015). *Phys. Rev. ST Accel. Beams*, **18**, 040703.

Ivanyushenkov, Y., Abliz, M., Boerste, K., Buffington, T., Doose, C., Fuerst, J., Hasse, Q., Kasa, M., Kim, S. H., Kustom, R. L., Lev, V., Mezentsev, N. A., Moog, E. R., Skiadopoulos, D., Syrovatin, V., Tsukanov, V., Trakhtenberg, E. M., Vasserman, I. B. & Xu, J. (2012). *IEEE Trans. Appl. Supercond.* **22**, 4100804.

Jia, Q., Zhang, S., Lu, S., He, D., Zhou, Q., Cao, Y., Dai, Z. & Zhao, Z. (2004). *Proceedings of the 26th International FEL Conference and 11th FEL Users Workshop*, 29 August–3 September 2004 Trieste, Italy, pp. 494–497.

Kim, S. H., Dejus, R. J., Doose, C., Kustom, R. L., Moog, E. R., Petra, M. & Thompson, K. M. (2003). *Proceedings of the 2003 IEEE Particle Accelerator Conference*, 12–16 May 2003, Portland, OR, USA, pp. 1020–1022.

Kostka, B., Rossmanith, R., Bernhard, A., Schindler, U. & Steffens, E. (2004). *Proceedings of the 3rd Asian Particle Accelerator Conference (APAC'04)*, 22–26 March 2004, Gyeongju, Korea, p. 221.

Mashkina, E., Grau, A., Baumbach, T., Bernhard, A., Casalbuoni, S., Hagelstein, M., Kostka, B., Rossmanith, R., Schneider, T., Steffens, E. & Wollmann, D. (2008*a*). *IEEE Trans. Appl. Supercond.* **18**, 1637–1640.

Mashkina, E., Kostka, B., Steffens, E., Grau, A., Casalbuoni, S., Hagelstein, M. & Rossmanith, R. (2008*b*). *Proceedings of the 11th Biennial European Particle Accelerator Conference (EPAC'08)*, Genoa, Italy, 23–27 June 2008, Genoa, Italy. WEPC121.

Moser, H. O. & Rossmanith, R. (2002). *Nucl. Instrum. Methods Phys. Res. A*, **490**, 403–408.

Tischer, M. & Pflueger, J. (2000). *TESLA-FEL Report 2000–08.* DESY, Hamburg, Germany.

Trakhtenberg, E., Ivanyushenkov, Y., Doose, C. & Kasa, M. (2010). *Diamond Light Source Proc.* **1**, e12.

Wallén, E. (2002). *Nucl. Instrum. Methods Phys. Res. A*, **495**, 58–64.

Wallén, E., Chavanne, J. & Elleaume, P. (2005). *Nucl. Instrum. Methods Phys. Res. A*, **541**, 630–650.